Pages: 92-109 / Vol. 17 / Issue 2 / Summer- Fall 2024

Journal of Aerospace Science and Technology

Journal Homepage: https://jast.ias.ir

Original Research Article

Experimental Assessment of the Airflow-Induced Vibration of a Single Cylinder with a Cantilever Beam

Reza Mahmoodpoor[1], Amir Kiyoumarsioskouei[2*], Amin Taraghi Osguei[3], Leila Donyaparast[4]

1,2, 3. Faculty of Mechanical Engineering, Sahand University of Technology, Tabriz, Iran and Institute of Applied Energy, Sahand University of Technology, Tabriz, Iran

4. Department of Mechanical Engineering, The University of Texas at Tyler, Tyler, USA

ARTICLE INFO

Received: 27 February 2024
Revised: 25 March 2024
Accepted: 29 March 2024
Available online: 29 March 2024

KEYWORDS:

Micro wind turbine
Vortex-Induced vibration
Galloping, Wake-Galloping
Low-Speed Wind Tunnel

ABSTRACT

Focus on different energy harvesting methods has led to various studies on the mechanism of flow-induced vibration phenomena, including vortex-induced vibration, galloping, and wake-galloping. In this study, an experimental investigation on flow around a cylinder with an elastic cantilever beam has been conducted to develop new energy harvesting devices based on its dynamic behavior. Therefore, the basic principles for the design of a high-resolution open-circuit subsonic wind tunnel were systematically studied and a specific small-scale wind tunnel was constructed based on the requirements. The test chamber cross section for the designed wind tunnel is square with a side length of 50 centimeters which can be used for investigation of different micro wind turbines performance up to velocity of 8 m/s with resolution of less than 0.1 m/s. The vibration of two prototype micro-turbines in the presence of obstacles and without obstacles has been studied in different Reynolds numbers. The results show that a circular cylinder oscillates with larger amplitude in the VIV range in comparison to the square cylinder, however, when galloping starts by increasing Reynolds number, the oscillation amplitude of the square cylinder severely increases. The experimental findings show that the presence of an obstacle upstream of the flow considerably increases the amplitude of oscillation, however, does not have a meaningful effect on the vibration frequency. Also, results indicate that the vibration amplitude of the bluff body in the wake-galloping phenomenon for the square obstacle is greater in comparison to the circular obstacle.

DOI: https://doi.org/10.22034/jast.2024.445963.1178

1 INTRODUCTION

Following the increase in waste generation, recycling is the first idea that comes to mind; however, some wastes are non-recyclable such as chemical batteries. Therefore, deploying a variety of well-developed and small-scale renewable components in electrical systems is a critical hot spot for researchers [1]. Various environmental energy sources, such as wind [2, 3], solar [4], thermal [5], mechanical [6], tidal [7], and others, are available with exploitable potential. Among these renewable energy sources, wind energy, or more broadly air flow, possesses a significant amount of

*Corresponding Author's Email: kiumarsi@sut.ac.ir

Print ISSN:1735-2134 Online ISSN: 2345-3648

mechanical energy and it also has various uses in the industry [8]. This energy can be converted into electrical energy through various energy harvesting mechanisms and utilized as electrical power in different systems. Utilizing ambient energy harvesting as a substitute power source for electronic devices, such as remote sensors, either in the biomedical field [9] or industry [10] has garnered significant attention in recent years. A flow-induced vibration (FIV) can occur due to flow-related phenomena in which vigorous ones can cause damage to any structure [11]. However, it can be discussed as the main source of energy in micro-electromechanical systems (MEMS) or wireless sensing systems [12].

FIV phenomena caused by flow such as wind and water could readily be harvested. For example, Zhu et al. [13] proposed a converter with a circular cylinder and a freely rotating pentagram impeller to harness energy from water currents. The structure of this converter helps hydrodynamic instability to affect the wider flow wake and unstable vortex shedding in case of enhancing the vibration and the generated power. Moreover, the DPEH proposed by Shan et al. [14], is an underwater converter in which two harvesters are arranged in series, hence by changing distances between them the output voltage and the effective output range of flow speed will significantly improve. Although 70% of the planet is covered by the ocean, the wind is one of the sources that is widely encountered in FIV systems. Accordingly, some researchers prefer to assess flow-induced vibration in wind tunnels. Maruai et al. [15] implemented a downstream flat plate in the wind tunnel to enhance the prospect of harvesting energy from the airflow. Shao et al. [16] studied the importance of cross-section geometries of bluff bodies in vibration amplitude in the wind tunnel. Also, they found that the arrangement of these bluff bodies in single and tandem configurations will affect the vibration amplitude as well. Fan et al. [17] represented different schemes of FIV for flexible multi-cylinders and tested them in a closed-loop wind tunnel. The harvesters were set in tandem, side-by-side, and staggered arrangements areas through which, four different regimes could be discussed. Additionally, Kiyoumarsioskouei and Taraghi Osguei [18] conducted multiple simulations to find the suitable geometry and arrangement for applying maximum force to the target cylinder from upstream cylinders. The results indicated that the square/circle configuration leads to relatively larger oscillatory forces. Among these studies, some researchers have decided to design and build a miniature wind tunnel. For example, Yang et al. [19] designed and built an aeroacoustics closed circuit wind tunnel with an open jet test chamber. The test chamber was made with a cross-section of 0.33 m2 and a flow velocity of 10 to 70 m/s. The design criteria along with detailed aerodynamic and aeroacoustics plans were presented. Validation tests were performed using a pitot tube, a hot-wire anemometer system, and a microphone. Aerodynamic and acoustic performance was compared with static data and the obtained results showed that the wind tunnel has high flow field quality and low background noise levels. Yakhshilikov and Inoyatkhodjaev [20] described the design and control techniques of an open circuit subsonic wind tunnel. The purpose of research was to design a wind tunnel with a wind velocity of 30 m/s and a test chamber with a cross-section of 0.25 m2. The axial fans available in the market were used to create the flow inside the wind tunnel and the pressure drop inside the wind tunnel was calculated with Computational Fluid Dynamics (CFD) and a PI controller was used to obtain smooth air flow and eliminate fluctuations in wind velocity. Biglete et al. [21] designed and installed a control system for an open circuit wind tunnel to monitor and check certain parameters for aerofoil testing, especially the angle of attack and wind velocity. Experiments were conducted to analyse the aerodynamic performance of an airfoil sample by determining the lift and drag forces applied to it. The sensors and electrical components of this test include: a pitot tube to read wind velocity, a fan to generate airflow, a servo motor to control the angle of attack of the airfoil, several load cells to read lift and drag forces, a smoke generator to observe the flow around the aerofoil, and finally a data logger to record real-time test data. Mauro et al. [22] investigated the design and test of a very small-scale wind tunnel. To verify the design criteria, a small-scale open-circuit wind tunnel was constructed. The test chamber had a square section of 25 cm2 and a flow velocity of about 6 m/s.

Flow-induced vibration energy harvesting systems need conventional mechanisms such as electromagnetic [23], piezoelectric [24, 25], electrostatic [26], dielectric [27], and triboelectric [28] to convert kinetic energy into usable energy. These microturbines can be used to supply electricity for electrical systems. On a small scale, these harvesters can act as an alternative power source for electronic systems instead of replacing

discharged batteries, equipment, and technology related to the Internet of Things (IoT), automatic wireless sensors, and sensors in telecommunication antennas that require low voltage [29].

In recent years, extensive research has been carried out on miniature wind turbines. However, in contrast to theoretical work, laboratory experiments are relatively limited, and more studies are needed to discuss different aspects of FIVs. This study not only evaluates the performance of micro-turbines with cylinders but also compares the dynamic behavior of two micro-turbines with similar physical specifications and hydraulic diameters such as circular and square bluff bodies. The study also investigates the effect of obstacle presence on the dynamic behavior of the harvester and the phenomenon of flow around the cylinder. The available wind tunnels were not suitable for conducting this experiment, as their cross-sections were small, and the wind resolution was not acceptable. Consequently, the need arose to construct an open-circuit wind tunnel, and a comprehensive roadmap for the design of various parameters of a wind tunnel is presented. In addition, the construction of a Cost-effective wind tunnel is presented, which facilitates other researchers in the field to have the necessary facilities for micro wind turbine experiments and conduct research with high precision. Another aim of the turbine tests was to investigate the effects of obstacles and vortex-induced vibrations (VIV) on energy harvesters. Therefore, three phenomena including VIV, galloping, and wake galloping were observed and compared in these experiments. This paper considers a new point to add to the similar previous research, in which placing an obstacle upstream of the flow in a wind tunnel may have a key role in these kinds of energy harvesters.

FIVs as environmentally friendly phenomena could be classified as VIVs, wake-galloping galloping, and flutter. In this paper, firstly the concept of each phenomenon characterized by FIVs will be described. Then, the experimental setup and the details of the tests are described in section 3. The experimental results are reported in section 4 and the conclusion is discussed in section 5.

2 PHENOMENA DESCRIPTION

According to demands, environmental conditions, and the amount of harvested power, the principle of FIVs energy harvesting can be divided into four categories as shown in Fig 1. VIV is a known phenomenon in fluid mechanics that can be seen when the flow faces an obstacle. When researchers are trying to harness energy with the minimum energy dissipation, they need to assess the optimal form of structure and mechanism for fulfilling this aim in VIV. One of these optimizations is adjusting the cross-section of bluff bodies [16] because the orientation of the bluff body with respect to the direction of the flow is important in calculations. The critical parameter in VIV is shedding frequency, f=US_t/L, where U is the velocity of the flow L is the characteristic length, and S_t S_tis the Struhaul number [30]. Mehmood et al. [31] studied a VIV-based energy harvester with a piezoelectric transducer in three different regimes namely pre-synchronization, synchronization, and post-synchronization regimes. Due to their numerical investigations, the synchronization region widens when the load resistance increases.

Galloping phenomena is the high-amplitude and low-frequency oscillation, in which, when the fluid passes bluff bodies, especially with edges and sharp corners could be observed. The importance of designing structures that produce significant renewable power by undergoing galloping oscillation is not hidden from researchers. Shao et al. and Yang et al. [16, 32] pointed out a comparative study of various cross-section profiles to identify the ideal bluff body. For the galloping energy harvester, adjusting conceptually the physics of the galloping mechanism can enhance the harvested power. For example, Sun et al. [33] investigated the GPEHAW device to optimize the performance of the system in both high and low wind velocity regimes.

Wake-galloping phenomena can be seen in unstable flow fields around downstream bluff bodies and this kind of harvester works similarly to VIV-based harvesters [34]. The wake-galloping phenomenon is caused by the vortex shedding of the upstream obstacle, which helps to harness higher voltages downstream. Subsequently, in these kinds of harvesters, the cross-section plays a key role in the final results. For example, Yan et al. [35] investigated energy harvesting from wake galloping of crescent-shape and D-shape cross-section bluff bodies inspired by the galloping of iced conductors. They used Hamilton’s principle, Euler–Bernoulli beam assumption, and the quasi-steady hypothesis to solve the harvested power density and numerically verified the experiment results.

In contrast to other flow-induced vibration phenomena, flutter is a “self-excited” oscillatory movement that is caused by the coupling of flow

forces with the elastic deformation of a structure. It is often the result of combined bending and torsion and affects plate-like structures such as splitter plates, airfoils, and suspension bridge decks. Unlike VIV and galloping, flutter can occur in structures with more than one degree of freedom. Therefore, the phenomenon of flutter helps the designers achieve higher capacities by better optimizing the interaction between the structure and the fluid [36].

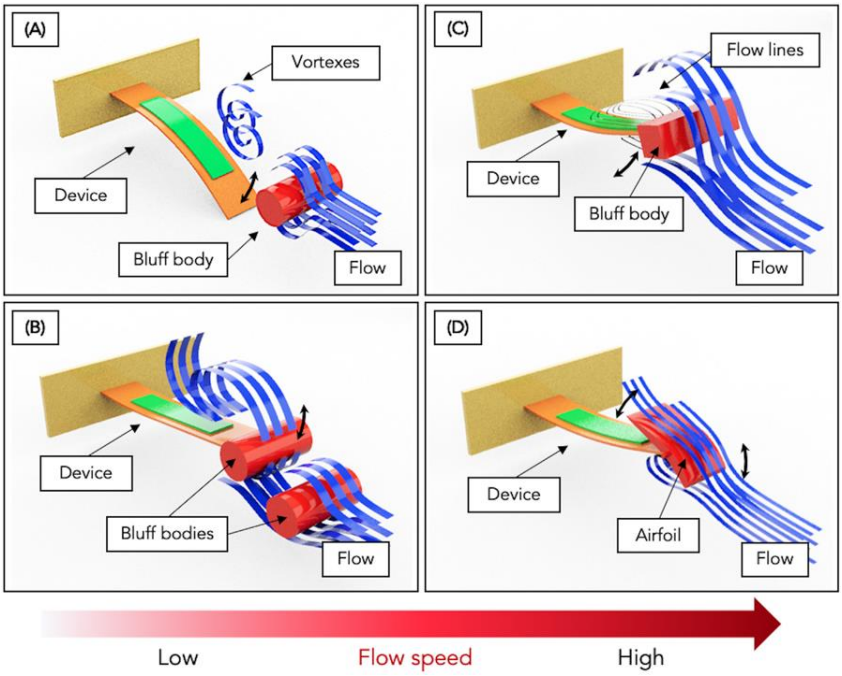

Fig. 1: Four categories of flow-induced vibration mechanisms classified by flow velocity range and physical characteristics: (A) vortex-induced vibrations, (B) wake-galloping, (C) galloping, and (D) flutter [37].

3 EXPERIMENT DESIGN

A scheme of an experimental model to investigate the performance of a micro-turbine in different Reynolds numbers to compare three different flow-induced vibration phenomena is represented in Fig 2. This setup consists of an open-circuit wind tunnel with a fan mounted at the end of the tunnel. The bluff body stands perpendicular to the direction of wind inside the wind tunnel. Additionally, a camera (60FPS), and a special ruler are employed to record the data and the hot wire port (GM8903) is installed to measure the wind speed

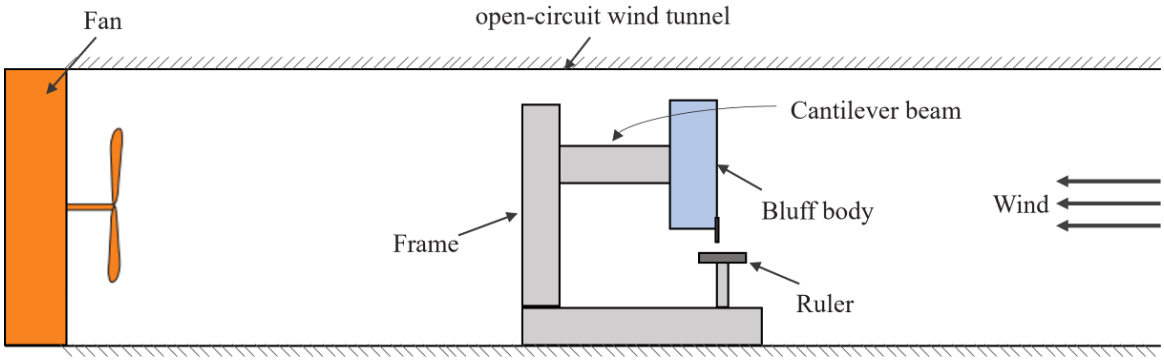

Fig. 2. Side view of schematic proposed micro-turbine along with the details.

3.1 Wind tunnel design and construction

In order to achieve a better resolution of wind velocity, especially at low velocities based on the main goal of this research, and also considering the economic limitations, firstly it was decided to design and construct a wind tunnel suitable for the current research as shown in Fig 3a, b. Wind tunnels can be classified according to their speed range, design limitations, the location of fans, etc. A wind tunnel has three-speed ranges: subsonic (Mach number less than one), transonic (Mach number equal to one), and supersonic (Mach number greater than one). On the other hand, various design limitations classify wind tunnels into two categories including open circuit (ambient air enters the wind tunnel through the nozzle and returns to the environment after passing through the test chamber and diffuser through the fan) and closed circuit (air circulates from the outlet of the fan to the beginning of the nozzle). However, there are two types of wind tunnels depending on the location of the fan. The suck-down wind tunnel creates a pressure drop at the exit of the tunnel, while the blower wind tunnel creates pressure at the entrance. In the next section, the principles behind the design of the Open Circuit Subsonic Suction Wind Tunnel will be explained and the step-wise design of this experiment will be described.

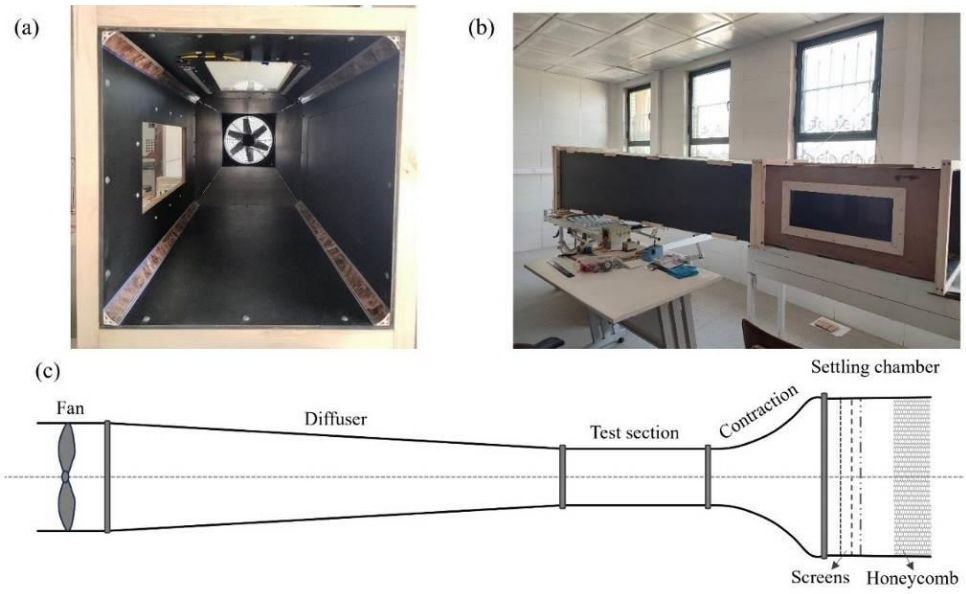

Fig. 3. Constructed open-circuit wind tunnel (a) the side, (b) front view (c) complete schematic of Wind Tunnel.

A typical wind tunnel consists of five main parts which will be explained by governing principles in the design of each section. As shown in Fig 3c, these five parts are the test section, diffuser, fan, contraction section, and settling chamber. The test section, diffuser, and fan of this wind tunnel are constructed based on the purpose of this study. Due to the physical dimension of the microturbines in the laboratory, as well as requirements for other tests that may be performed in the future, the cross-sectional dimensions of the test section are considered first. In the same way, the next step is determining the length of the test chamber according to equation 1 and then designing and constructing the diffuser. In the design and construction of the diffuser, in addition to the relations used, it is necessary to observe the physical limitations of the fans in the market. Finally, the design and construction of the contraction section is the final step of the wind tunnel.

3.1.1 Test section

The test section as the location of setup in the wind tunnel is the main part of a wind tunnel. A wind tunnel cross-section is designed based on three main parameters, which include the shape, the dimensions, and the linear velocity inside the chamber. Wind tunnel parameters are directly related to the test type and purpose. Ideally, the test section should be circular with no sharp edges so that the boundary layer does not thicken and airflows do not separate. For better durability, a square section with 45-degree chamfered corners is recommended [22]. To

calculate the length of the test section, equation 1 can be used after selecting the dimensions for the cross-section of the test section. Accordingly, $L_{ts}$the length of the test section and D_h the hydraulic diameter of the cross-section vary depending on the cross-section shape [20].

$$0.5D_h \leq L_{ts} \leq 3D_h \quad (1)$$

The test section length should be between 0.5 to 3 times the hydraulic diameter. As a result, the incoming airflow is almost uniform and the boundary layer does not separate at the exit of the test section. For the creation of uniform flow, the airflow exiting the contraction must take a path at least 0.5 times the hydraulic diameter, and lengthening the test section beyond 3 times the hydraulic diameter may increase boundary layer thickness [38]. According to Fig 4a, a test chamber with a square cross-section and a side length of 50 cm was constructed due to the length of available wind micro-turbines in the laboratory which are between 20 and 40 cm. Equation 2 was used to determine the length of the test chamber, therefore, doubling the hydraulic diameter gives 100 cm for the length of the test chamber.

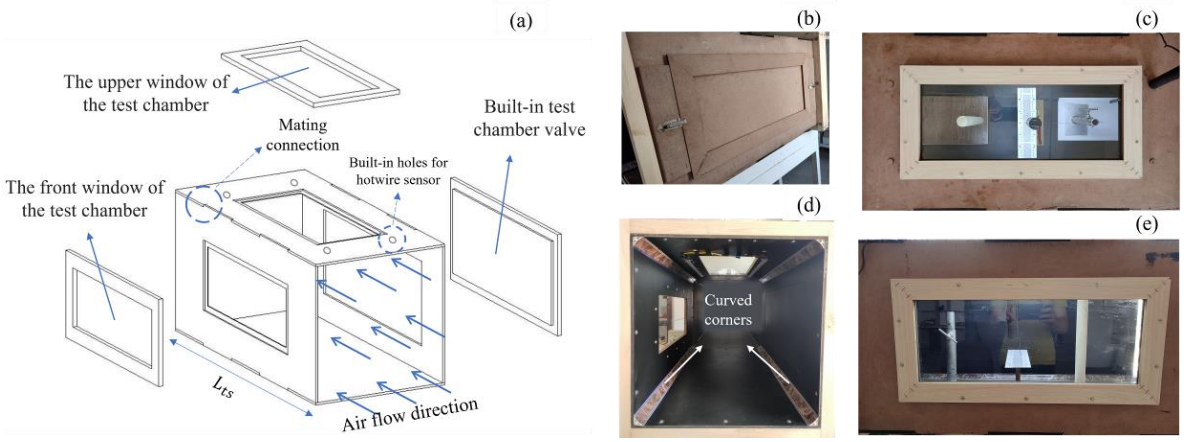

Fig. 4. (a) Exploded diagram of test chamber components, connection and sensor installation locations, and different views of the constructed test chamber: back (b), top (c), interior (d), and front (e).

$$L_{ts} = 2D_h \quad (2)$$

Fig 4a shows a door at the backside and two windows at the front and top which make it easier to place the micro-turbines, observe, and record the test data. Raw 8-millimeter MDF sheets were used to create the desired design, and curved profiles were used to eliminate sharp corners. A laser-cutting device was used to cut different components of the test chamber. Using a CNC machine, the location for installing the glass panels has been floor-inlaid to a thickness of 4 mm for better positioning. Finally, the glass frame is attached to the test chamber's body using bolts and foam to prevent air from escaping. Fig 4b, c, d, e shows different views of the test chamber from various perspectives.

3.1.2 Diffuser

Through the diffuser, the speed of outgoing airflow is reduced by expanding so that its pressure reaches the ambient pressure, which increases the efficiency of the wind tunnel. The design of a diffuser begins with its inlet, where the dimensions and shape of the cross-section are known. The outlet of a diffuser in an open circuit wind tunnel coincides with the fan in size and shape and the inlet and outlet cross sections are calculated by equation 3. An interface element should be used if the cross-sections of the connected areas differ [39]. According to equation 3, ratios less than 2 lead to an irregular flow velocity caused by swirling flow due to the rotation of the fan blades as shown in Fig 5. However, ratios greater than 3 increase the dimensions and the total cost of the wind tunnel. It is recommended to use the ratio of 2 for the cross-section area.

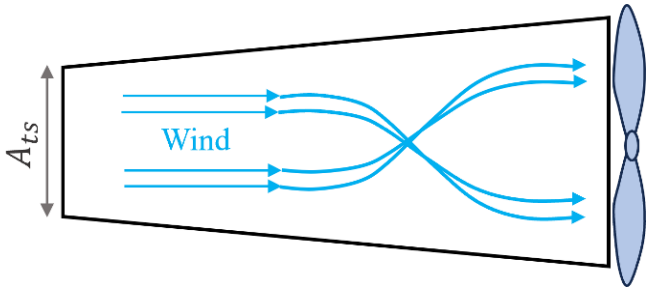

Fig. 5. Swirling flow due to the rotation of fan blades.

$$2 \leq \frac{A_{fan}}{A_{ts}} \leq 3 \quad (3)$$

Usually, the expansion angle based on inlet and outlet cross-sections is used to calculate the length of the diffuser. According to the principles of design in ultrasonic diffusers, the expansion angle of the cone should not pass the maximum value of 6 degrees and the minimum value of 2 degrees. Very long diffusers (expansion angle less than 2°) lead to pressure losses along the path, and angles greater than 5° increase outlet pressure recovery, which can lead to boundary layer separation and ultimately unsteady flow. According to the design of the National Aerodynamic Complex at the NASA Ames Research Center, it is recommended to use a cone expansion angle of 4 degrees [22, 38, 40, 41]. The length of the diffuser can be obtained by solving equation 4,5 after determining the expansion angle of the cone and the hydraulic diameter of the inlet section of the diffuser [40].

$$AR = \frac{A_{fan}}{A_{ts}} \quad (4)$$

$$\frac{\theta}{2} = tan^{-1}\left(\frac{1}{2}\left(\frac{\sqrt{AR}-1}{\frac{L_d}{D_h}}\right)\right) \quad (5)$$

Where L_d and θ are the length of the diffuser and the cone expansion angle, respectively. According to equations, and assuming the cross-section area of the diffuser in the outlet to be square, its side length would be approximately 71 cm for the cross-sectional area coefficient of 2.

As previously mentioned, it's essential to determine the fan's dimensions before constructing the output section of the diffuser. In order to construct the diffuser, we've taken into account the dimensions of the fan, which includes an outlet cross-section with a side length of 72.5 cm and a length of 297 cm. At the outset and end of the diffuser, we've incorporated two wooden frames to enhance its structural integrity. Furthermore, the four corners of the diffuser's sides have been designed to interlock, similar to the construction method used for the test chamber. For a visual representation of the various components of the diffuser, refer to Fig 6a. To construct the diffuser, we employed two 8 mm MDF sheets and incorporated two wooden frames at both the initial and terminal sections. Given the substantial size of these components, a CNC machine was utilized for their fabrication. It's worth mentioning that, when using a CNC machine, any inclined inner edges must be manually corrected. In order to enhance the diffuser's robustness, we introduced four wooden angle bars at the outer corners of the structure, as depicted in Fig 6c. Additionally, the inner corners of the diffuser were sealed using silicone glue.

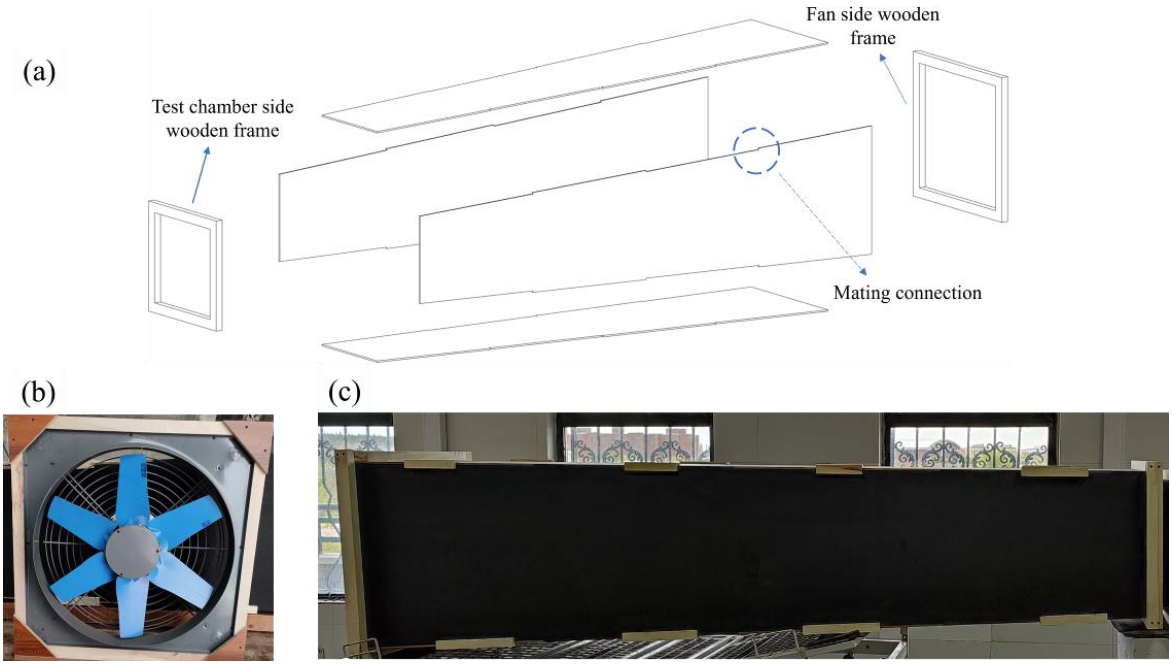

Fig. 6. (a) Expanded diagram of diffuser components and a picture of (b) the fan and (c) the diffuser.

3.1.3 Fan

Airflow inside the wind tunnel is created using a fan. Equation 6 is used to determine the average velocity of airflow in different sections of the wind tunnel, where the mass conservation law and area ratio are considered. Therefore, according to the required flow rate in the test section, the fan flow rate can be calculated.

$$V_i A_i = V_j A_j \tag{6}$$

In wind tunnel design, the fan is typically connected to the end of the diffuser after the diffuser has been designed. In the process of designing a wind tunnel and according to the equations, the outlet cross-section area of the diffuser must be calculated based on the cross-section area of the test section. However, during the construction of the wind tunnel, due to the constraints of the physical dimensions of fans available in the market, the nearest fan in size to the calculated outlet cross-section area of the diffuser should be provided. Subsequently, the diffuser is constructed based on the dimensions of the fan.

In this research, a three-phase alternating current, electric motor fan has been used as the power source in accordance with the aforementioned hypotheses. Table 1 includes additional technical details of the fan.

Table 1. Characteristic parameters of used fan in constructed wind tunnel.

parameter	value
Voltage	360 V
Power	410 W
Motor speed	139 rpm
Flow	8300 m^3/h
Current	0.90 A
Frequency	50 Hz
Weight	16.4 Kg

In order to connect the fan to the end of the diffuser section more easily, a wooden frame with a cross-section of 4×4.5cm is made and installed on the fan according to Fig 6b. This allows wood to be connected to wood rather than wood to metal during wind tunnel construction.

As shown in Fig 7, the wind tunnel consists of three general parts, which are the test section, fan, and diffuser. To connect these three components, bolt, and nut connections were utilized along with a sealing layer. This method of connection simplifies the transportation and maintenance of various sections of the wind tunnel.

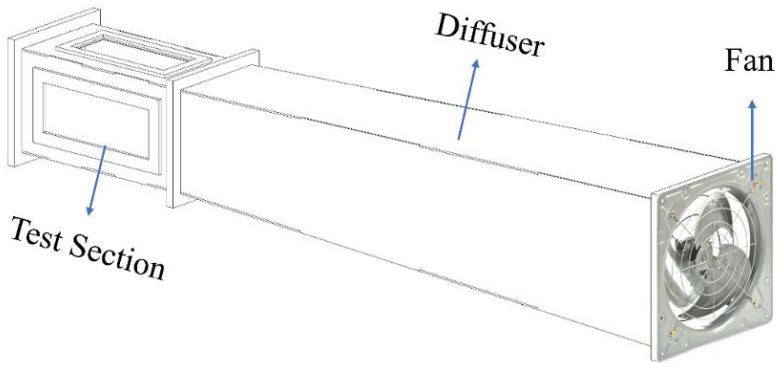

Fig. 7. A complete plan of the different parts of the wind tunnel.

3.1.4 Contraction

The contraction accelerates the flow rate and creates a uniform flow rate profile at the entrance of the test section. A parameter called contraction cross-sectional area ratio is used to design the inlet cross-section of the contraction section. According to equation 7, the ratio of the cross-section of the contraction should be in the range of 6 to 10. Using a cross-sectional area ratio of fewer than 6 leads to a high-pressure loss in the upstream parts of the wind tunnel, while ratios higher than 10 cause an excessive increase in the inlet cross-section dimensions. Therefore, it is desirable to take the contraction cross-sectional area ratio equal to 7, which represents a good balance between dimensions and performance [39].

$$6 \leq \frac{A_n}{A_{ts}} \leq 10 \tag{7}$$

According to Fig 8 and the study of Bell and Meta [39], the ratio of contraction length to twice its semi-side length should be between 0.667 and 1.79 according to equation 8. One can approximately put this ratio equal to one 1 for calculation.

$$0.667 \leq \frac{L_n}{2y_0} \leq 1.79 \quad (8)$$

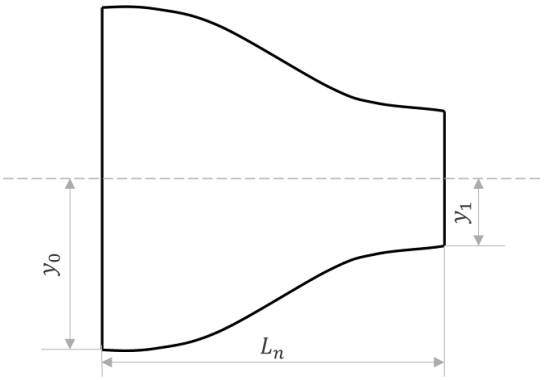

Fig. 8. Schematic of nozzle used in wind tunnel.

Considering the experimental tests carried out by Bell and Meta [39], ratios less than 0.667 lead to the separation of the airflow before the contraction of the outlet section, and ratios greater than 1.79 lead to an increase in the thickness of the boundary layer. Therefore, using equation 8 the total length of the contraction is calculated. Since the profile of the longitudinal section of the contraction is curved, the Nozzle silhouette profile is created using the fifth-order Bell-Metta polynomials [39]. The curved walls of the contraction section, minimize turbulence and flow separation, and as a result, make the inlet flow uniform and smooth to the test section. The curved walls help to gradually decrease the cross-sectional area of the flow, thereby increasing the air velocity while reducing the likelihood of boundary layer separation and flow disturbances. Contrary to the mentioned cases, the flat walls can lead to an increase in turbulence and irregular flow and decrease the accuracy of the measurements, but it is obvious that in cases where the turbulence does not have much importance on the test results, flat walls can also be used. Equation 9 shows the mathematical equation of the fifth-order polynomials of Bel-meta.

$$y = a_1\xi^5 + a_2\xi^4 + a_3\xi^3 + a_4\xi^2 + a_5\xi + C \quad (9)$$

In equation 9, the value of ξ can be obtained from equation 10, with the values of *x* that are mentioned in the range of equation [22].

$$\xi = \frac{x}{L_n} \quad , \quad 0 \leq x \leq L_n \quad (10)$$

If we consider the inlet semi-side-length of the contraction y_0 and its outlet semi-side-length y_1, the Bel-Meta polynomial coefficients will be equal to Table 2.

Table 2. Bell-meta polynomial coefficients [22].

Coefficients	Amounts
a_1	$-18.99\ (y_1 - y_0)$
a_2	$1.669\ (y_1 - y_0)$
a_3	$18.33\ (y_1 - y_0)$
a_4	0
a_5	0
C	y_0

3.1.5 Settling chamber

The flow entering the wind tunnel is not necessarily horizontal and uniform, and in many cases, the flow velocity vector has vertical components or turbulency that are not efficient for aerodynamic tests [40]. The purpose of the settling chamber is to create a Straight flow, with less turbulence and more uniformity [42]. According to Fig 9a, the settling chamber has two subsections of honeycomb and screens.

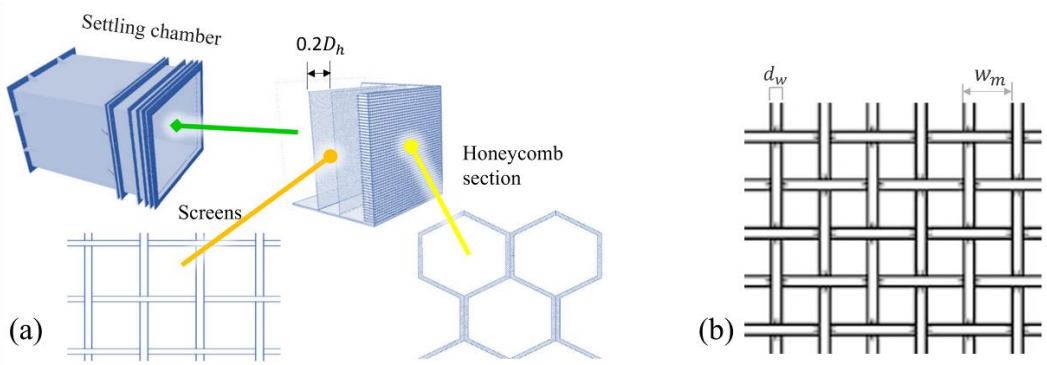

Fig. 9. Schematic of different parts of the settling chamber (a) [20] and wire mesh sample (b).

In order to reduce the fluctuations in the inlet velocity, a honeycomb with cells aligned with the flow direction is used. In a honeycomb, the flow yaw angles should not be more than 10 degrees, because larger yaw angles cause the stall in honeycomb cells and thus decrease efficiency and increase power loss [43].

The honeycomb porosity parameter (β_h) is used to design the honeycomb section (equation 11), [44]. So A_{flow} and A_{total} are the actual flow level and the total cross-sectional area, respectively.

$$\beta_h = \frac{A_{flow}}{A_{total}} \geq 0.8 \tag{11}$$

The screens are interwoven metal wires (may also be nylon or polyester) that form square grids. Screens mainly reduce the flow velocity fluctuations by creating a static pressure drop proportional to the square (quadratic power) of the velocity, with little effect on the flow direction, which consequently reduces the thickness of the boundary layer [43, 45]. According to Prandtel [46], a series of screens with different mesh quality is more efficient than a single screen in reducing turbulency. To check the effectiveness of screens, a factor called screen porosity (β_s) is used and it is defined according to equation 12 [38, 47]. Where A_{flow} is the actual flow area and A_{total} is the total area. The effectiveness of screens in reducing turbulence is strictly related to their porosity, which should be in the range of 0.8 - 0.58 [43]. The reason for choosing the lower limit of the range is related to the consideration of flow instability and the upper limit of the range is related to turbulence control [46].

$$0.58 \leq \beta_s = \frac{A_{flow}}{A_{total}} \leq 0.8 \tag{12}$$

According to Fig 9b and ρ_w as the wire density, the relationship of the porosity of the screens can be rewritten in terms of other parameters and according to equation 13. Finally, with the help of equation 14, it is possible to design the screens required in the construction of the containment chamber [42].

$$\rho_w = \frac{n_w}{L_{sc}} = \frac{1}{W_m} \tag{13}$$

$$\beta_s = (1 - d_w \rho_w)^2 \tag{14}$$

The distance between the screens (shown in Fig 9a) should be such that the fluid is completely recovered from the turbulence caused by the previous screens before reaching the next screens [42-44]. Therefore, it is recommended to use a distance $0.2D_h$ between the screens [43].

3.2 Micro-turbine setup

As shown in Fig 10 this micro-turbine consists of a rigid stand with a height of 39cm and a flexible cantilever beam made of steel which in this experiment, also plays the role of a splitter with a fixed end. Its length is set to 18.5cm with a width of 4cm and a thickness of 0.5mm. In addition, there are two bluff bodies with different cross-sections. Here, the diameter of square and circular cross-sections is set to 4cm for both bluff bodies; Moreover, the height of the bluff bodies is 17.1cm. Using two different cross-sections in this experiment is expected to affect the phenomena. It is expected that the phenomenon caused by wind stream in the presence of the square bluff body will be similar to the galloping phenomenon, and the circular one will be like VIVs.

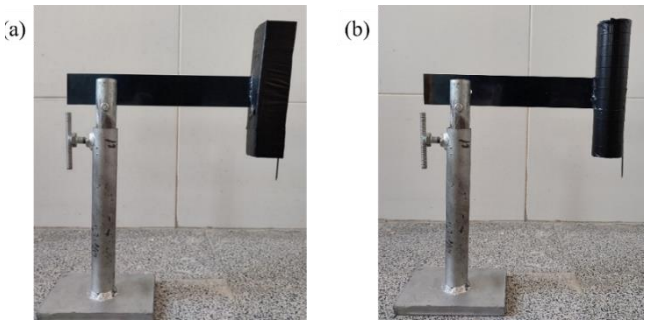

Fig. 10. Micro-turbine setup with square (a) and circular (b) cross-section bluff bodies.

In the following investigation, in order to create a wake galloping phenomenon, an obstacle will be placed in front of the bluff body for a further experiment. The locations of micro-turbines and test equipment are detailed in Fig 11.

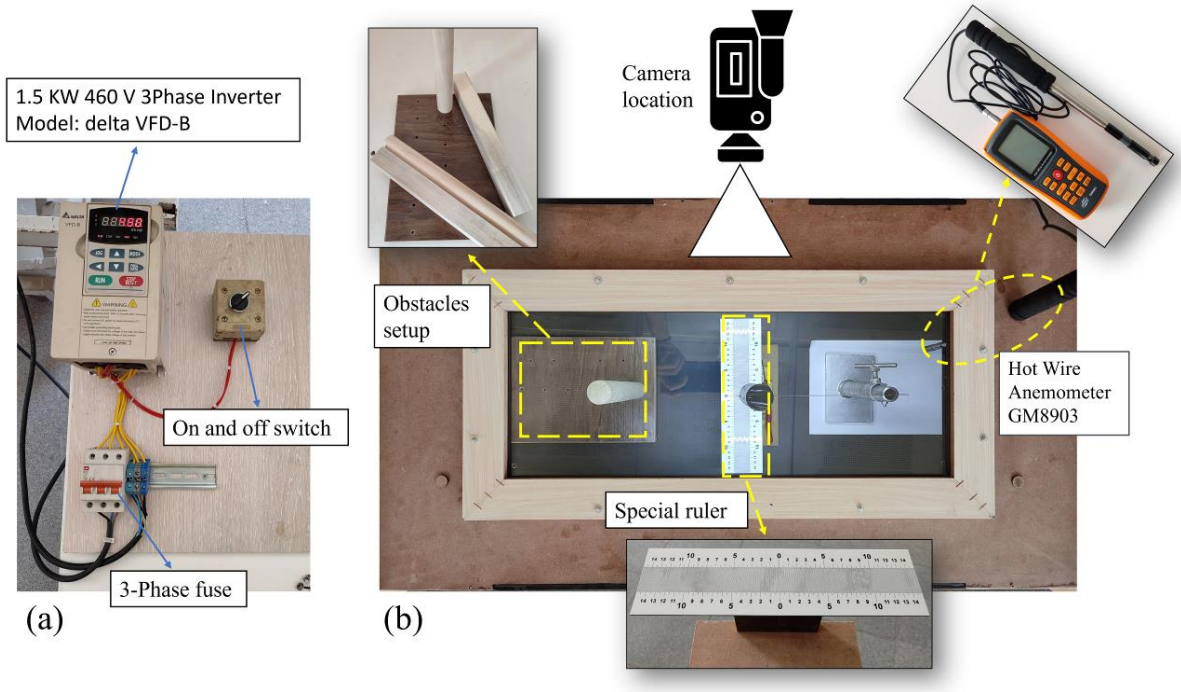

Fig. 11. (a) control and electrical equipment of the wind tunnel, which includes an inverter, a three-mode switch, and a three-phase fuse. (b) the top view of the test chamber, including the micro-turbine, the video camera, the hot wire sensor, the obstacle setup, and a special ruler.

As can be seen in Fig 11 (top view of the test chamber), after placing the micro-turbine and a special ruler, a camera recording 60 frames per second was mounted exactly above the ruler to record the vibrations of the bluff body. To measure the wind speed behind the micro-turbine, a hot wire flow meter sensor was used, which was inserted through prepared holes on the left and right sides of the turbine. Obstacles can also be added to or removed from the experiment as required. A three-phase 1.5 kW Delta inverter model VFD-B was used to start and control the fan speed. A switch with three operating modes switches the fan on and off, both as a blower and as a suck-down fan.

3.3 Parameters and measurement procedure

This test needs some parameters to be measured. Firstly, as a result of the air stream inside the tunnel, the flow speed is determined by measuring the average of six points that are illustrated in Fig 12. Also, According to observations, points 2 and 5 were the closest points to the average fluid velocity. By determining flow speed, the Reynolds number can be obtained according to $Re = UL/\nu$, where L is the characteristic length and ν is the kinematic viscosity which is equal to $1.5 \times 10^{-5}(m^2/s)$.

The oscillations induced in the bluff body of micro-turbines during this experiment are primarily the result of the bending or torsion of their flexible beam. Fig 13 can be used for a better understanding of these two phenomena. Fig 13b illustrates the oscillation of a bluff body due to the torsion of its cantilever beam, while Fig 13c shows the oscillation of a bluff body due to the bending of its cantilever beam.

Using the special ruler and image processing, the displacements of the bluff body can be measured when the flow excites it. Thus, the micro-turbines maximum displacement (X_{max}) is obtained. By recording this oscillation over a period of time the turbine oscillation frequency is obtained $f = 1/T$. Finally, the other important parameter is the Strouhal number which is used in fluid dynamics to describe the mechanism of fluctuating fluid flow and can be calculated from $St = fL/U$, where f, L, and U are the frequency of vortex shedding, the characteristic length, and fluid speed, respectively. To extract the research results first of all, two tests were performed to check the oscillation range of the microturbines and the cantilever beam effect connected to the bluff bodies. For this purpose, first, the number of tests for each case was extracted and the interval of the tests was divided using inverter

frequency, (each case was tested at 10 different frequencies). After the initial review of the results, the parts that were likely to cause FIV phenomena were divided into smaller intervals and the results related to each microturbine were depicted by performing the final test. The behavior of each of the square and circular bluff bodies in different Reynolds numbers and the phenomena caused by these bluff bodies were studied. Tests without obstacles were designed to study the phenomena of VIV and galloping, whereas tests with obstacles were designed to study the phenomenon of wake galloping. So, three more tests were conducted to investigate the improvement of the oscillation range of the microturbine with a circular bluff body, in order to check the effect of obstacles with different cross-sections on the oscillation range of microturbines and compare it with other researchers' results. Following these experiments, three other experiments were also conducted to investigate the effect of different bluff bodies on the frequency range of microtubules. Finally, the effect of the beam length on the oscillation range and the possibility of increasing the oscillations at low Reynolds, as well as its effect on the frequency range, were investigated and tested. The logic of the selected intervals for each experiment was that in the investigation of the behavior of the phenomena, the intervals were selected with a larger number and close to each other to observe the continuous and smoother oscillating behavior of the harvesters and in investigating the effect of different parameters on the amplitude of oscillation, intervals were done with a small number and greater distance from each other to better understand the effect of each phenomenon. To further ensure the correctness of the answers, three tests were taken from each interval, and finally, the average of these three answers was reported, with the help of these three tests, the error bar was drawn for each graph.

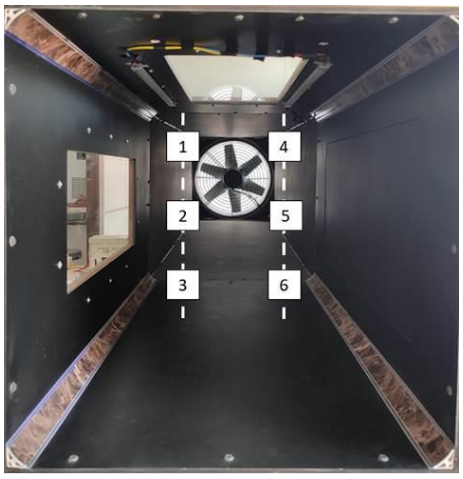

Fig. 12. The flow speed is calculated in Six points that are shown inside the tunnel.

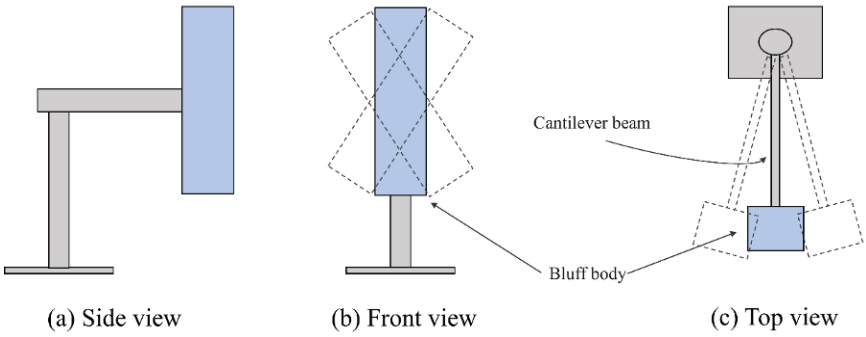

Fig. 13. (a) Schematic, oscillation caused by (b) torsion and (c) bending of the micro-turbine by its cantilever beam.

4 RESULTS

Through this setup, the vibrational behavior of the micro-turbines due to airflow was studied in different Reynolds numbers as well as the length of the cantilever beam. Moreover, in our setup, the relation between the fan's inverter frequency and average flow velocity inside the test section is almost linear as depicted in Table 3.

The results of this research are divided into three general categories: first is investigating the oscillating behavior of micro-turbines with different bluff bodies, second is investigating the effect of different obstacles on the performance of these types of micro-turbines and hence studying the wake galloping, and finally is the effect of beam length on the amplitude of oscillation. To improve the accuracy of the behavior of the micro-turbine frequency diagram, large samples were employed and all experiments were repeated at least three times.

Table 3. Obtained inverter frequencies according to different flow speeds and Reynolds number.

Inverter Frequency (Hz)	$U_{avg}(m/s)$	Reynolds number
2	0.26	693.33
3	0.43	1146.67
4	0.6	1586.67
4.5	0.61	1637.33
5	0.68	1805.33
5.5	0.71	1890.67
6	0.85	2256
7	1.01	2693.33
8	1.13	3000
10	1.21	3224
15	1.94	5176
20	2.81	7493.33
25	3.32	8848
30	4.53	12072
35	4.7	12538.67
45	5.78	15408
60	7.58	20210.67

4.1 Oscillation of the bluff body

The performance of the micro-turbine with a circular bluff body can be considered as the mechanical part of an FIV micro-turbine where an elastic beam is attached to the bluff body. According to this test, micro-turbine oscillates in three different regimes, namely, VIV, steady, and galloping. Fig 14a shows the oscillating behavior of this micro-turbine in three different regimes. In this division, the VIV section refers to a range of oscillations in which the microturbine reaches an oscillation peak and then the oscillation range decreases. In the galloping phenomenon by increasing the wind velocity or Reynolds number, the range of oscillation increases accordingly and finally, a remaining section between these two fluctuating phenomena, which is neither VIV nor galloping, and the amplitude of the fluctuations is very small or torsional, is called the steady range.

According to Fig 14 and the data obtained from the experimental observations during the test, the vibration of the bluff body at the approximate Reynolds number of 700 is negligible. As the Reynolds number increases, so does the vibration range of the micro-turbine. As a result, the Reynolds number rises to 1891 with the fluid velocity of 0.71 m/s reaching its relative maximum oscillation. Then, it starts to decrease, and at the Reynolds number between 3000 to 5000, the oscillation amplitude of the object is almost ignorable. Note that, the recorded numbers of 1 or 2 mm are the immediate effect of vibration on the bluff body or torsion of its trail (cantilever beam) instead of bending, as described in Fig13. For Reynolds above 12000, the bluff body oscillation amplitude increases with the fluid velocity. Accordingly, three oscillation regimes are, initially, VIV phenomena that occurred at Reynolds numbers around 700 to 3000. This is followed by a slight change known as the steady-state region at Reynolds numbers between 3000 and 5000. Next, the galloping phenomena at Reynolds numbers more than 5000 are observed. To better observe the behavior of this micro-turbine, the diagram of Fig 14b is drawn in logarithmic form and the three oscillation regimes of this micro-turbine are shown in this figure.

The micro-turbine with a square cross-section bluff body has only shown a galloping phenomenon due to its sharp corners. According to Fig 14c, d, the oscillation amplitude of this micro-turbine is less than 5 mm at the Reynolds number range of 700 to 3000. However, at the Reynolds number about 3000, an amplitude jump of 14 mm has happened. At high Reynolds, due to the limitation in the flexible beam displacement and the increase of the opposite bending force, the slope of the displacement-Reynolds diagram decreases. This is while for the circular bluff body, due to the small amount of displacements, the slope of the diagram increases significantly with the increase of the Reynolds number.

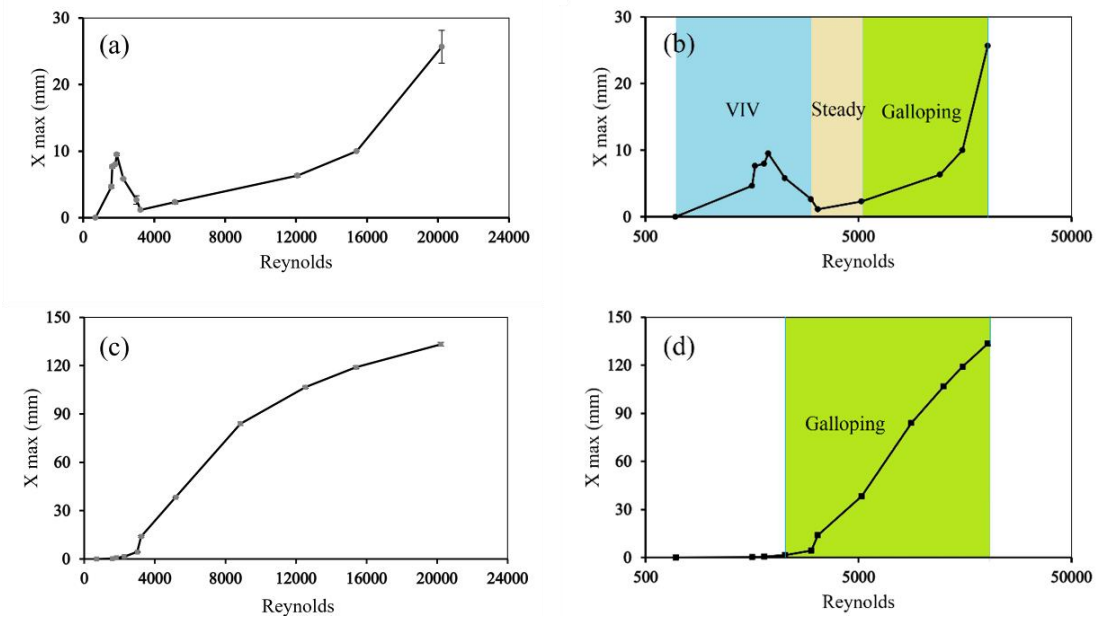

Fig. 14. Oscillation amplitude of the bluff body with the (a) circular and (c) square cross-section cylinder and also the Logarithmic form of the oscillation amplitude for both circular (b) and square (d) bluff body in different Reynolds numbers.

Based on the observation of the oscillatory behavior of two types of micro-turbines and comparing the results, it is confirmed that the micro-turbine with a square bluff body has a better performance at high speeds and a larger amplitude than that of the micro-turbine with a circular bluff body. The intersection of these two graphs is between the Reynolds numbers 2200 to 3000. Also, similar to Zhao et al. [48] and Yang et al. [32] studies, it is observed that the bluff body with a square section has the highest outer power because X_{max} is much larger than the cylindrical bluff body. For a better understanding of the difference between the behavior of these two micro-turbines at different Reynolds numbers, the graph comparing the behavior of these two micro-turbines is shown in Fig 15.

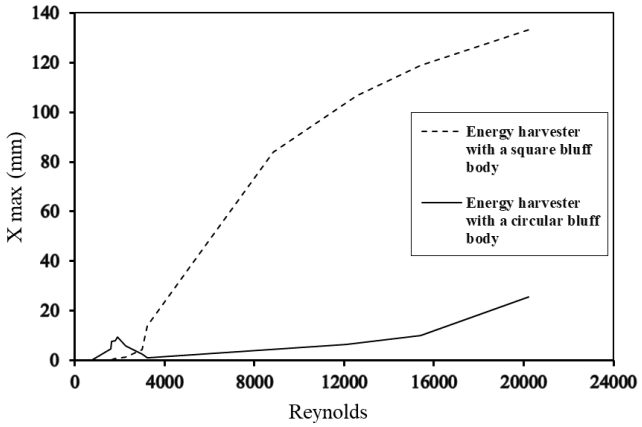

Fig. 15. Comparison of oscillatory behavior of circular and square bluff body micro-turbine.

4.2 Investigation on wake galloping phenomenon

Abdelkefi et al. [49] found experimentally that the development of wake galloping effects in harvesters results in increasing outer power. According to Fig 16a, by comparing the results of the micro-turbine with the circular bluff body without and with the various obstacles, it is observed that the presence of obstacles can cause an increase in the oscillation amplitude at Reynolds greater than 3400 by creating wake effects. However, at Reynolds numbers less than 3400, it causes a reduction in the oscillation range compared to the unobstructed state, because the fluid does not have enough energy to form powerful wakes. It is also observed that at higher Reynolds numbers (Reynolds numbers greater than 15000), the impact of the wake effects gradually decreases, and the oscillation range in obstructed and unobstructed states becomes closer to each other. Two different obstacles with a square and circular cross-section in the 20 cm distance upstream of every micro-turbine's bluff body were used. Experimentally, these tests showed that the effect of the square obstacle is a little bit greater than the cylindrical obstacle in the oscillation range. Owing to that, the most significant effect of obstacles in increasing the oscillation amplitude occurred at the Reynolds number of around 15500, so the circular obstacle increased the oscillation amplitude by 100% and the square obstacle by 113.3%.

Furthermore, in Fig 16b, it is observed that whether with or without the obstacle, with the increase in Reynolds number, the frequency of micro-

turbine remained relatively unchanged. This can be due to the fact that in the galloping flow regimes, the frequency of the oscillations is more of a structural parameter and is less dependent on the flow regime.

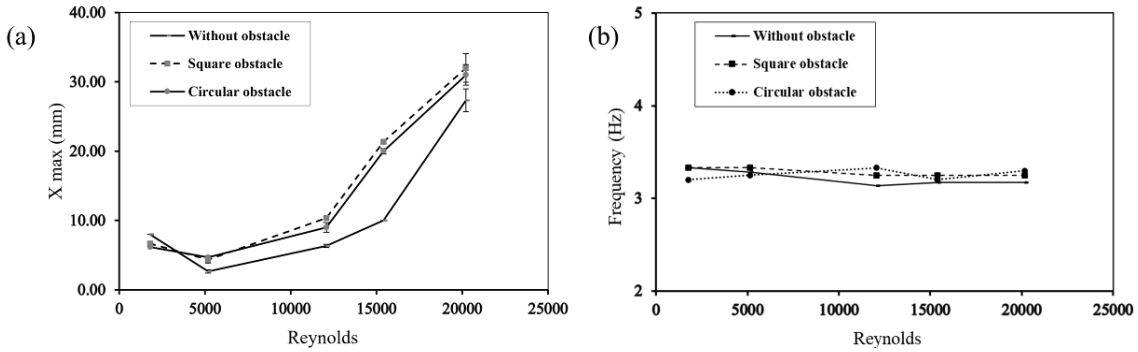

Fig. 16. Comparison of oscillation amplitude changes in the presence of with and without the obstacle for the circular bluff body (a) and micro-turbine frequency changes over different Reynolds numbers (b)

4.3 The effect of elastic beam length on oscillation amplitude

According to the tests conducted at the Reynolds number of 8848, and 5 different lengths using the micro-turbine with a square bluff body and a steel flexible cantilever beam length: 10, 15, 20, 25, and 30 cm. It is better to explain that, at Reynolds numbers higher than 9000, due to reaching the physical limitations of the experiment, data became either unrecordable or subject to increased measurement error and at lower Reynolds numbers, the range of oscillation changes was smaller and less noticeable. According to this experimental validation, the oscillation amplitude increase is well in agreement with increasing the length of the plate. Fig 17 shows that the length of the plate has an inverse relation with the stiffness of the cantilever; and as a result, it has an inverse relation with the system's frequency. According to this diagram, it can be concluded that it is possible to reach higher amplitudes than the maximum amplitude at lower frequencies by increasing the beam length.

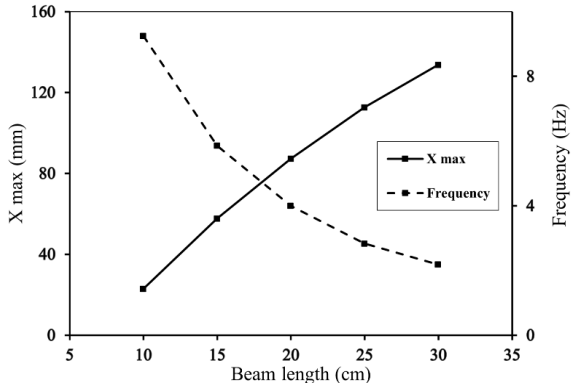

Fig. 17. The relationship between beam length, oscillation amplitude, and the micro-turbine oscillating frequency in the galloping-based micro-turbine at Reynolds 8848.

With an overview of the results of the experiment, it can be said that the micro-turbine fluctuated with the circular bluff body in three regimes of VIV, Steady, and galloping. With the increase of Reynolds number, the micro-turbine started to fluctuate from the position of stillness and reached the maximum amplitude in the Reynolds of 1890, and then again, the amplitude of the fluctuations decreased to near stillness. Afterward, the micro-turbine reached the steady region, in which there were no fluctuations caused by the bending of the cantilever beam, and the observed slight fluctuations were the result of the torsion of the beam. According to the experimental observations, crossing over the steady region, although the increase in the Reynolds number caused the increase in the amplitude of the fluctuations, the quality of the fluctuations based on the bending of the beam has decreased gradually, which means the fluctuations were the outcome of both bending and torsion of the cantilever beam. These interpretations lead to the conclusion that the micro-turbine with the circular bluff body can perform better in laminar flow and low Reynolds number. In contrast, the micro-turbine with the square bluff body, which is based on the galloping phenomenon, has followed a fixed behavior. As the Reynolds number increased, the amplitude of the fluctuations increased until the physical limits of the micro-turbine were reached. The registered fluctuations in this micro-turbine were mainly the result of the bending of the cantilever beam in all ranges of these fluctuations. The fluctuation amplitude of the micro-turbine with the circular bluff body was only better at Reynolds below 3000, and at Reynolds above 3000, the fluctuation

amplitude of the micro-turbine with the square bluff body was consistently higher.

In order to improve the amplitude of the micro-turbine fluctuations with the circular bluff body, different obstacles were used which caused an acceptable increase in the fluctuations' amplitude in the Reynolds higher than 3400. The quality of the bending fluctuations going throw the VIV regime decreased similarly. In general, the fluctuations were the result of the bending and torsion of the bluff body cantilever beam. Also, the impact of the square obstacle on the fluctuation amplitude specifically in the higher Reynolds, was relatively more than the circular obstacle.

Finally, to increase the fluctuation amplitude in the galloping phenomena (micro-turbine with the square bluff body) in laminar flow and low Reynolds (especially in the Reynolds lower than about 3200) the length of the bluff body cantilever beam could be increased, which causes the decrease of the frequency of the micro-turbine.

5 CONCLUSION

In this paper, experimental tests are performed to interpret energy harvesting from three different FIV phenomena including VIV, galloping, and wake-galloping. Therefore, two bluff bodies with different cross-sections are investigated at different Reynolds in the range of 700 to 20000. Additionally, the effect of obstacle and length of flexible beam on the vibration amplitude of micro-turbine have been investigated. The following conclusion can be drawn based on the observations:

1. For the circular bluff body connected to the elastic beam three different phenomena including VIV, steady flow, and galloping are observed, however, for the square bluff body with an elastic splitter plate only galloping occurred.
2. With increasing the Reynolds number, the amplitude of oscillation for the square bluff body experienced a dramatic rise in comparison with the circular bluff body.
3. Locating circular and square obstacles upstream of the flow has a significant effect on the amplitude of the oscillations at high Reynolds by changing galloping to wake galloping phenomenon.
4. The change in the length of the cantilever beam is directly related to the amplitude of the oscillation but is inversely proportional to the frequency.

In summary, a square cylinder bluff body generates a permissible vibration amplitude at high Reynolds values by galloping. However, if a circular cylinder is to be used, an obstacle is required for the circular cylinder to generate strong vibrations by wake-galloping.

CONFLICT OF INTEREST

The authors declare that they have no conflict of interest.

REFERENCES

[1] L. . Zhao and Y. Yang, "Toward small-scale wind energy harvesting: Design, enhancement, performance comparison, and applicability," *Shock and Vibration*, vol. 2017, 2017, https://doi.org/10.1155/2017/3585972.

[2] Y. Kumar, J. Ringenberg, S. S. Depuru, V. K. Devabhaktuni, J. W. Lee, E. Nikolaidis, B. Andersen, and A. Afjeh, "Wind energy: Trends and enabling technologies," *Renewable and Sustainable Energy Reviews*, vol. 53, pp. 209–224, 2016, https://doi.org/10.1016/j.rser.2015.07.200.

[3] S. E. Hosseinidoost, A. Sattari, M. Eskandari, D. Vahidi, P. Hanafizadeh, P. Ahmadi , "Techno-Economy Study of wind energy in Khvaf in Razavi Khorasan Province in Iran, " *J. Comput. Appl. Mech.*, vol. 47, no. 1, pp. 53–66, 2016, https://doi.org/10.22059/jcamech.2016.59255.

[4] N. Kannan and D. Vakeesan, "Solar energy for future world: A review," *Renew. Sustain. Energy Rev.*, vol. 62, pp. 1092–1105, 2016, https://doi.org/10.1016/j.rser.2016.05.022.

[5] G. Sebald, D. Guyomar, A. Agbossou, "On thermoelectric and pyroelectric energy harvesting," *Smart Mater. Struct.*, vol. 18, no. 12, 2009, Art. no. 125006, https://doi.org/10.1088/0964-1726/18/12/125006.

[6] H. Pan, L. Qi, Z. Zhang, J. Yan , "Kinetic energy harvesting technologies for applications in land transportation: A comprehensive review," *Appl. Energy*, vol. 286, 2021, Art. no. 116518, https://doi.org/10.1016/j.apenergy.2021.116518.

[7] Z. Lin and Y. Zhang, "Dynamics of a mechanical frequency up-converted device for wave energy harvesting," *J. Sound Vib.*, vol. 367, pp. 170–184, 2016, https://doi.org/10.1016/j.jsv.2015.12.048.

[8] M. A. Ardekani, F. Farhani, M. Mazidi , "Effect of wind on thermal performance of Heller dry cooling tower," *J. Comput. Appl. Mech.*, Vol. 45, No. 1, pp. 1-8, 2014.

[9] L. Donyaparastlivari, M. Atmeh, P. Indic, A. Ibrahim , "A feasibility analysis of triboelectric energy harvester for hip implants," in *Proc. 2023 IEEE 16th Dallas Circuits and Systems Conf. (DCAS)*, pp. 1, 2023, https://doi.org/10.1109/DCAS57389.2023.10130245.

[10] M. Mukherjee, L. Shu, R. V. Prasad, D. Wang, G. P. Hancke , "Sleep scheduling for unbalanced energy harvesting in industrial wireless sensor networks," *IEEE Commun. Mag.*, vol. 57, no. 2, pp. 108–115, 2019, https://doi.org/10.1109/MCOM.2019.1700811.

[11] X. Xia, L. Zhou, Z. Wang, D. Liu, "Effects of trailing-edge modification of guide vanes on the wake vortices under different inflow conditions," *Proc. Inst. Mech. Eng. A, J. Power Energy*, vol. 235, no. 8, pp. 1892–1901, 2021, https://doi.org/10.1177/09576509211017434.

[12] J. Wang, G. Zhao, M. Zhang, Z. Zhang, "Efficient study of a coarse structure number on the bluff body during the harvesting of wind energy," *Energy Sources, Part A: Recovery, Utilization, and Environmental Effects*, vol. 40, no. 15, pp. 1788–1797, 2018, https://doi.org/10.1080/15567036.2018.1486916.

[13] H. Zhu, Y. Zhao, T. Zhou , "CFD analysis of energy harvesting from flow induced vibration of a circular cylinder with an attached free-to-rotate pentagram impeller," *Appl. Energy*, vol. 212, pp. 304–321, 2018.

[14] X. Shan, H. Li, Y. Yang, J. Feng, Y. Wang, T. Xie, "Enhancing the performance of an underwater piezoelectric energy harvester based on flow-induced vibration," *Energy*, vol. 172, pp. 134–140, 2019, https://doi.org/10.1016/j.energy.2019.01.120.

[15] N. M. Maruai, M. S. Mat Ali, M. H. Ismail, S. A. Z. Shaikh Salim, "Downstream flat plate as the flow-induced vibration enhancer for energy harvesting," *J. Vib. Control*, vol. 24, no. 16, pp. 3555–3568, 2018, https://doi.org/10.1177/1077546317707877.

[16] Z. Shao, T. Zhou, H. Zhu, Z. Zang, W. Zhao , "Amplitude enhancement of flow-induced vibration for energy harnessing," in *Proc. 6th Int. Conf. Renewable Energy Technol. (ICRET 2020)*, vol. 160, E3S Web Conf., 2020, Art. no. 01005, https://doi.org/10.1051/e3sconf/202016001005.

[17] X. Fan, Z. Wang, X. Chen, Y. Wang, W. Tan "Experimental investigation on flow-induced vibration of flexible multi cylinders in atmospheric boundary layer," *Int. J. Mech. Sci.*, vol. 183, 2020, Art. no. 105815, https://doi.org/10.1016/j.ijmecsci.2020.105815.

[18] A. Kiyoumarsioskouei, A. Taraghi Osguei, "Time and frequency analysis of fluctuating hydrodynamic forces acting on circular and square cylinders in laminar flows ," *J. Braz. Soc. Mech. Sci. Eng.*, vol. 45, 2023, Art. no. 295, https://doi.org/10.1007/s40430-023-04220-y.

[19] Y. Yang, Y. Liu, R. Liu, C. Shen, P. Zhang, R. Wei, X. Liu, P. Xu, "Design, validation, and benchmark tests of the aeroacoustic wind tunnel in SUSTech," *Appl. Acoust.*, vol. 175, 2021, Art. no. 107847, https://doi.org/10.1016/j.apacoust.2020.107847.

[20] J. Yakhshilikov, J. Inoyatkhodjaev, "Design And Control Techniques Of The Open-Circuit Subsonic Wind Tunnel With Closed Testing Section," *Acta of Turin Polytechnic University in Tashkent*, vol. 10, no. 4, pp. 65–70, 2020.

[21] E. R. Biglete, M. C. E. Manuel, M. B. Cardone, Y. L. Manuel, M. L. M. Pilar, J. R. S. Santos, J. C. D. Cruz, M. S. Verdadero, Design and Installation of a Control System for an Open-Circuit Wind Tunnel," in *Proc. IEEE 12th Int. Conf. HNICEM*, Manila, Philippines, pp. 1–6, 2020 https://doi.org/10.1109/HNICEM51456.2020.9400153.

[22] S. Mauro, S. Brusca, R. Lanzafame, F. Famoso, A. Galvagno, M. Messina, "Small-scale open-circuit wind tunnel: Design criteria, construction and calibration," *Int. J. Appl. Eng. Res.*, vol. 12, no. 23, pp. 13649–13662, 2017.

[23] M. El-Hami, P. Glynne-Jones, N. White, M. Hill, S. Beeby, E. James, A. Brown, J. Ross, "Design and fabrication of a new vibration-based electromechanical power generator," *Sensors and Actuators A: Physical*, Vol. 92, No. 1-3, pp. 335-342, 2001, https://doi.org/10.1016/S0924-4247(01)00569-6.

[24] X. Zheng, L. He, S. Wang, X. Liu, R. Liu, G. Cheng ,"A review of piezoelectric energy harvesters for harvesting wind energy," *Sens. Actuators A Phys.*, vol. 351, 2023, Art. no. 114190, https://doi.org/10.1016/j.sna.2023.114190.

[25] R. Hosseini, M. Nouri, "Shape Design Optimization of Unimorph Piezoelectric Cantilever Energy Harvester," *J. Comput. Appl. Mech.*, vol. 47, no. 2, pp. 247–259, 2016, https://doi.org/10.22059/jcamech.2017.224975.126.

[26] Y. Chiu, C.-T. Kuo, Y.-S. Chu, "MEMS design and fabrication of an electrostatic vibration-to-electricity energy converter r," *Microsyst. Technol.*, vol. 13, pp. 1663–1669, 2007, https://doi.org/10.1007/s00542-006-0348-z.

[27] C. Zhang, Z. Lai, X. Rao, J. Zhang, D. Yurchenko, "Energy harvesting from a novel contact-type dielectric elastomer generator," *Energy Convers. Manag.*, vol. 205, 2020, Art. no. 112351,https://doi.org/10.1016/j.enconman.2019.112351.

[28] Z. Ren, L. Wu, Y. Pang, W. Zhang, R. Yang, "Strategies for effectively harvesting wind energy based on triboelectric nanogenerators," *Nano Energy*, vol. 100, 2022, Art. no. 107522, https://doi.org/10.1016/j.nanoen.2022.107522.

[29] R. mahmoodpoor, A. kiyoumarsioskouei, A. Taraghi Osguei, "Small scale wind turbines: A state of the art review," *J. Renew. New Energy*, vol. 11, no. 2, pp. 176–187, 2024, https://doi.org/10.22034/jrenew.2024.190797.

[30] M. S. Pantazopoulos, "Vortex-induced vibration parameters: critical review," in *Proceedings of the Vortex-Induced Vibration Parameters Conference*, 1994.

[31] A. Mehmood, A. Abdelkefi, M. Hajj, A. Nayfeh, I. Akhtar, A. Nuhait, "Piezoelectric energy harvesting from vortex-induced vibrations of

circular cylinder," *Journal of Sound and Vibration*, vol. 332, no. 19, pp. 4656-4667, 2013, https://doi.org/10.1016/j.jsv.2013.03.033.

[32] Y. Yang, L. Zhao, L. Tang, "Comparative study of tip cross-sections for efficient galloping energy harvesting," *Applied Physics Letters*, Vol. 102, No. 6, 2013, https://doi.org/10.1063/1.4792737.

[33] W. Sun, J. Seok, "Novel galloping-based piezoelectric energy harvester adaptable to external wind velocity," *Mechanical Systems and Signal Processing*, Vol. 152, 2021, Art. no. 107477, https://doi.org/10.1016/j.ymssp.2020.107477.

[34] J. Wang, L. Geng, L. Ding, H. Zhu, D. Yurchenko, "The state-of-the-art review on energy harvesting from flow-induced vibrations," *Applied Energy*, Vol. 267, 2020, Art. no. 114902, https://doi.org/10.1016/j.apenergy.2020.114902.

[35] Z. Yan, L. Wang, M. R. Hajj, Z. Yan, Y. Sun, T. Tan, "Energy harvesting from iced-conductor inspired wake galloping," *Extreme Mechanics Letters*, vol. 35, 2020, Art. no. 100633, https://doi.org/10.1016/j.eml.2020.100633.

[36] Y. Chen, X. Mu, T. Wang, W. Ren, Y. Yang, Z. L. Wang, C. Sun, A. Y. Gu, "Flutter phenomenon in flow driven energy harvester–A unified theoretical model for "stiff" and "flexible" materials," *Scientific Reports*, Vol. 6, 2016, Art. no. 35180, https://doi.org/10.1038/srep35180.

[37] M. Mariello, F. Guido, V. M. Mastronardi, F. Madaro, I. Mehdipour, M. T. Todaro, F. Rizzi, M. De Vittorio, "Micro-and nanodevices for wind energy harvesting," in: *Nano Tools and Devices for Enhanced Renewable Energy*, Eds., pp. 291-374: Elsevier, 2021.

[38] J. B. Barlow, W. H. Rae, A. Pope , *Low-Speed Wind Tunnel Testing*, 3rd ed., John Wiley & Sons, 1999.

[39] J. H. Bell, R. D. Mehta, "Contraction design for small low-speed wind tunnels," NASA-CR-177488, 1988.

[40] A. Teseletso, M. Namoshe, N. Subaschandar, S. Kutua, "Design of an Open-circuit Subsonic Wind Tunnel for Educational Purpose," *Proceedings of the Botswana Institution of Engineers (BIE) 14th Biennial Conference*, 2015.

[41] P. T. Zell, "Performance and test section flow characteristics of the National Full-Scale Aerodynamics Complex 80- by 120-Foot Wind Tunnel," NASA-TM-103920, 1993.

[42] Q. Y. Nguyen, "Designing, constructing, and testing a low–speed open–jet wind tunnel," *International Journal of Engineering Research and Applications*, vol. 4, no. 1, pp. 243-246, 2014.

[43] R. D. Mehta, P. Bradshaw, "Design rules for small low speed wind tunnels," *The Aeronautical Journal*, vol. 83, no. 827, pp. 443-453, 1979, https://doi.org/10.1017/S0001924000031985.

[44] M. Arifuzzaman, M. Mashud, "Design construction and performance test of a low cost subsonic wind tunnel," *IOSR Journal of Engineering*, vol. 2, no. 10, pp. 83-92, 2012.

[45] B. Joglekar, R. M. Mourya, "Design, construction and testing open circuit low speed wind tunnel," *International Journal of Engineering Research and Reviews*, vol. 2, no. 4, pp. 1-9, 2014.

[46] L. Prandtl, "Attaining a steady air stream in wind tunnels," *NACA-TM-726*, 1933.

[47] M. S. Genç, İ. Karasu, H. H. Açıkel, " An experimental study on aerodynamics of NACA2415 aerofoil at low Re numbers," *Experimental Thermal and Fluid Science*, vol. 39, pp. 252-264, 2012, https://doi.org/10.1016/j.expthermflusci.2012.01.029.

[48] L. Zhao, L. Tang, Y. Yang, "Small wind energy harvesting from galloping using piezoelectric materials," *Smart Materials, Adaptive Structures and Intelligent Systems*, pp. 919-927, 2013, Art. no. SMASIS2012-8212, https://doi.org/10.1115/SMASIS2012-8212.

[49] A. Abdelkefi, J. M. Scanlon, E. McDowell, M. R. Hajj, "Performance enhancement of piezoelectric energy harvesters from wake galloping," *Applied Physics Letters*, vol. 103, no. 3, 2013, https://doi.org/10.1063/1.4816075.

COPYRIGHTS
Authors retain the copyright and full publishing rights.
Published by Iranian Aerospace Society. This article is an open access article licensed under the Creative Commons Attribution 4.0 International (CC BY 4.0).

HOW TO SITE THIS ATRICLE

R. Mahmoodpoor, A. Kiyoumarsioskouei, A. Taraghi Osguei, L. Donyaparast, "Experimental Assessment of the Airflow-Induced Vibration of a Single Cylinder with a Cantilever Beam," *Journal of Aerospace Science and Technology*, Vol. 17, Issue 2, 2024, pp. 92-110.

DOI: https://doi.org/10.22034/jast.2024.445963.1178

URL: https://jast.ias.ir/article_193280.html